The ARAUCARIA Project: VLT-FORS spectroscopy of blue supergiants in NGC 3109 – Classifications, first abundances and kinematics[1]

C. J. Evans[2], F. Bresolin[3], M. A. Urbaneja[3], G. Pietrzyński[4,5], W. Gieren[4] and R.-P. Kudritzki[3]

Received _____; accepted _____

Accepted by ApJ

[1]Based on observations at the European Southern Observatory Very Large Telescope in programme 171.D-0004.

[2]UK Astronomy Technology Centre, Royal Observatory, Blackford Hill, Edinburgh, EH9 3HJ, UK

[3]Institute for Astronomy, 2680 Woodlawn Drive, Honolulu, HI 96822

[4]Universidad de Concepción, Departamento de Fisica, Astronomy Group, Casilla 160-C, Concepción, Chile

[5]Warsaw University Observatory, Al. Ujazdowskie 4, 00-478, Warsaw, Poland

ABSTRACT

We have obtained multi-object spectroscopy of luminous blue supergiants in NGC 3109, a galaxy at the periphery of the Local Group at ∼1.3 Mpc. We present a detailed catalog including finding charts, V and I magnitudes, spectral classifications, and stellar radial velocities. The radial velocities are seen to trace the rotation curves obtained from studies of the H I gas. From quantitative analysis of eight B-type supergiants we find a mean oxygen abundance of 12 + log(O/H) = 7.76 ±0.07 (1-sigma systematic uncertainty), with a median result of 7.8. Given its distance, we highlight NGC 3109 as the ideal example of a low metallicity, dark-matter dominated, dwarf galaxy for observations with the next generation of ground-based extremely large telescopes (ELTs).

Subject headings: stars: early-type – stars: fundamental parameters – galaxies: individual: NGC 3109 (DDO236) – galaxies: stellar content

1. Introduction

NGC 3109 is a Magellanic-like spiral galaxy of type SBm (de Vaucouleurs et al. 1991) at the outer edge of the Local Group, at a distance of 1.3 Mpc (Capaccioli et al. 1992; Lee 1993; Soszyński et al. 2006). Its relative proximity and low foreground reddening (Burstein & Heiles 1984) make it well-suited to exploring galaxy formation and evolution in dwarf irregulars beyond the Magellanic Clouds.

Photometric studies have suggested that the main body of NGC 3109 has a low, SMC-like metal abundance (Elias & Frogel 1985; Greggio et al. 1993). Moreover, from deep imaging, Greggio et al. noted subtly different populations across the disk of the galaxy that they ascribed to different metallicities/star-formation histories in their target fields, to differential reddening, or a combination of both. The galaxy is thought to have a very metal-poor stellar halo (Minniti et al. 1999), although Demers et al. (2003) have argued that the minor axis star counts can be explained by the inclination of the disk, rather than requiring a significant halo population. There also appears to be evidence of interaction with the Antlia dwarf galaxy ∼1 Gyr ago (Barnes & de Blok 2001).

Observations of the rotation curve of NGC 3109 suggest a dominant dark-matter halo (Jobin & Carignan 1990), that cosmological N-body cold dark matter (CDM) simulations have struggled to reproduce (Navarro et al. 1996). NGC 3109 has also lent itself to tests of the predictions of Modified Newtonian Dynamics (MOND, Milgrom 1983). but observational uncertainties such as the adopted distance led to differing conclusions (Lake 1989; Milgrom 1991). Improved observational data (e.g. Blais-Ouellette et al. 2001) have helped the situation, but the debate continues (e.g. Valenzuela et al. 2006,and references therein).

As part of the larger ARAUCARIA project (P.I. Gieren) we have obtained spectroscopy of some of the most visually-luminous stars in NGC 3109, using the Very Large Telescope (VLT) of the European Southern Observatory (ESO). These are the first spectroscopic observations of resolved stars in this galaxy, enabling us to study the kinematics and abundances of the young stellar population in this dark-matter dominated dwarf. The observations are detailed in Section 2, followed by classification of the spectra in Section 3. Stellar radial velocities are presented in Section 4, in which we have compared them with H I rotation curves, and in Section 5 we undertake a quantitative analysis of eight stars to investigate their chemical abundances. Lastly, in Section 6 we suggest NGC 3109 as a target for future large telescopes.

2. Target Selection and Observations

The data were taken with the FORS2 (focal-reducer and low dispersion spectrograph) instrument at the VLT on 2004 February 24 & 25. The multi-object spectroscopy with moveable slits (MOS) mode of operation was used with the 600B grism for the blue-region observations and the 1200R grism in the red. Targets were selected from V and I-band photometry obtained as part of the ongoing Cepheid variable search programme at the Las Campanas Polish 1.3-m telescope (Pietrzyński et al. 2006). In conjunction with new J and K-band VLT observations, these data have been used to obtain a distance to NGC 3109 of 1.30 ± 0.02 Mpc (Soszyński et al. 2006), the most precise distance estimate to date.

Figure 1 shows the location of our targets in the colour-magnitude diagram. Secondary targets were also observed serendipitously in some slitlets; the spectra of these were also extracted when reducing the data. This is the origin of the redder targets in Figure 1, in particular the G-type supergiant with $(V - I) \sim 1.7$.

Finding charts from the FORS V-band pre-imaging are given in Figures 2, 3, and 4. For reference, the three strongly-saturated stars in Figure 2 are those near the 'F2' label in Figure 1 from Bresolin et al. (1993). Moving eastwards from the three reference stars, the FORS fields roughly span the F2, F1, D2 and D1 fields from Bresolin et al. Note the slight 'drift' northeastwards in the astrometry for the targets in the western part of Figure 3. These were selected from a different FORS pre-image, but the offset of the target stars is evident from the isolated bright targets. Stars #4, 45 and 61 were secondary targets that happened to be in the CCD gap in the pre-image. Our fields also overlap with the imaging from Greggio et al. (1993). The western quarter of Figure 2 is in their region C, and nearly all of our targets shown in Figure 3 are encompassed by their region A.

Prior to extraction of the spectra, the L.A.COSMIC routines from van Dokkum (2001) were used to clean the frames of cosmic rays. The spectra were then bias corrected, extracted and wavelength calibrated using IRAF[1] (v2.12). An optimal extraction was used for the blue spectra, but we employed a simpler summed extraction routine for the red data – we prefer this method as nebular and/or intrinsic emission at Hα can sometimes lead

[1]IRAF is distributed by the National Optical Astronomy Observatories, which are operated by the Association of Universities for Research in Astronomy, Inc., under cooperative agreement with the National Science Foundation.

to problems with sky-subtraction when using optimal extractions. Indeed, accurate sky subtraction is still challenging in those stars with strong, nearby nebula emission. Further manipulation of the spectra was done with the Starlink package DIPSO, including correction to the heliocentric frame and rectification.

The observations are summarised in Table 1. In Table 2 we list the observational details for each star, by column these are: (1) Running identifier; (2) FORS field of observation; (3) Right Ascension; (4) Declination; (5) V magnitude; (6) $V - I_c$ colour; (7) Spectral type; (8) Radial velocity in kms^{-1}; (9) 1-σ uncertainty of radial velocity; (10) Number of absorption lines measured in determination of the radial velocity; (11) Signal-to-noise ratio of the spectrum near to Hγ; (12) Additional comments such as cross-identifications with other catalogues (e.g. Sandage & Carlson 1988), or presence of strong nebular emission lines.

The FWHM resolution (as defined by the arc lines) for the 600B data is approximately 4.6 Å, corresponding to 3.2 pixels. For the 1200R spectra this is 6.1 Å (3.1 pixels). These both give a spectral resolving power R of ∼1,000. As a consequence of the MOS slitlets the exact wavelength coverage varies, but the λ3650 to λ5550 Å region is covered by all of the blue spectra.

2.1. Photometric variability

The photometry from Pietrzyński et al. (2006) was primarily obtained to monitor Cepheid variables so we have 70 to 80 photometric observations of each of our stars. The data were acquired over two seasons, with three-quarters of them from the first season (spanning Julian Dates 2452343 to 2452359).

The V magnitudes and $(V - I_c)$ colours in Table 2 are the means of the multi-epoch values. The expected scatter of the photometric results at a given magnitude is illustrated by Figure 2 from Pietrzyński et al. (2006), in which their photometry is compared to that from Hidalgo et al. (in preparation). At $V \sim 18$ there is excellent agreement, with an increasing scatter toward fainter magnitudes (of order $\pm 0.1^m$ at $V = 20$).

We find evidence for variability ($>0.1^m$) in 5 of our targets that are brighter than $V = 20$, as shown in Figure 5. To give an indication of the scatter of the individual measurements, the lightcurve of a non-variable star (#7) is also shown. There may be

small-scale periodic (or aperiodic) variations in our other targets that are undetected from qualitative inspection, but these are not explored further here.

3. Spectral Classification

With previous studies suggesting that the metallicity of NGC 3109 is comparable to that of the SMC (e.g. Elias & Frogel 1985), the FORS spectra were classified by comparison to published SMC spectra. For B-type supergiants we use the SMC standards published by Lennon (1997), and for A- and later-type stars we use the criteria from Evans & Howarth (2003) and Evans et al. (2004). These sources have already tackled the issue of classification at low metallicities in the MK system. For O-type spectra we rely on the digital atlas of Walborn & Fitzpatrick (1990), with reference to the SMC data presented by Walborn et al. (2000).

In addition to the low foreground reddening, the total line-of-sight reddening is also relatively low for stars in the major axis of NGC 3109, with E($B-V$) ∼0.14 (Davidge 1993). From the O star spectra shown in Figure 6 it can be seen that there is some contamination of the spectra by interstellar Ca K and H (at λ3933 and λ3968 respectively, with the latter blended with Hϵ at λ3970). The intensity of the interstellar components are comparable to those seen in some SMC spectra (compare with the O-type spectra shown in Figure 2 from Evans et al. 2004), and should not strongly affect the classifications for the A-type spectra – particularly as the intensity of the metallic absorption lines is also considered when classifying.

The resolution from FORS (∼4.5 Å in the blue) is lower than that usually used for precise classification. We have taken this into account when classifying the spectra (largely by degrading the standards to the same effective resolution). Classifications for our targets are given in Table 2.

For spectra with signal-to-noise ratios of greater than 50, we show the blue-region data (λ3900 to λ4750 Å) in Figures 6 to 12. To highlight the spectral sequence more clearly, there is deliberate repetition of some spectra.

3.1. Comments on individual stars

We now give further explanation of our adopted spectral types for some of the targets that display peculiar or interesting features, non-unique types etc.

#2 – mid Be – Figure 10: There is significant emission in the Balmer series in this spectrum. The intensities of the He I and Mg II lines are consistent with a mid B-type classification (of ∼B3-5), although of course there may be infilling in the helium lines, and/or continuum effects from a circumstellar disk. There is weak [N II] emission in the wings of the Hα profile (see Figure 13), but the scale and extent of the Hα emission suggests a primarily non-nebular origin, hence the Be-type classification.

#7 – B0-1 Ia – Figure 7: The uncertainty in this spectral type arises from what appears to be very weak He II λ4542. The spectrum is otherwise consistent with that of a B1-type supergiant.

#9 – B0.5 Ia – Figure 7: This bright star has a nearby companion (cf. Figure 2) to the extent that the spatial profiles were somewhat blended prior to extraction. The dominant spectrum appears to be that of a B0.5 supergiant, with weak He II λ4686 absorption.

#12 – B8 Ia – Figure 10: The blue spectrum of star #12 shows increasing amounts of infilling in Balmer lines as one moves redwards, presumably from a stellar outflow. The Hα profile displays broad and strong emission (with an equivalent width of 7.5 ±0.3 Å).

#22 – B1 Ia – Figures 7 & 8: From qualitative inspection the N II λ3995 line in this spectrum appears relatively strong for its type (but see comment in Section 5).

#24 – B2-3 Iab – Figure 9: The absence of Si III combined with Mg II absorption (albeit weak) requires a type of B3. However there is also weak absorption from O II λ4650 that would not usually be expected, suggesting a slightly earlier type.

#35 – O8-9.5 I(f) – Figure 6: The strength of the He II λ4542 absorption is consistent with an earlier type than the λ4200 line, leading to a range of possible classifications for this spectrum. Weak N III emission is seen at $\lambda\lambda$4634-40-42, with infilled He II λ4686.

#36 – mid B – Figure 10: P Cygni emission is seen in both the Hγ and Hβ lines; similarly at Hα (Figure 13). The ratio of Si II $\lambda\lambda$4128-32 to He I λ4121 requires a mid to late B-type classification for this spectrum, well matched by the other He I lines. However the weakness of the Mg II λ4481 feature contradicts this somewhat, suggesting a slightly earlier type.

#59 – B0-3 – Figure 9: Weak absorption is seen from Si III but a precise spectral type cannot be assigned due to the absence of other diagnostic lines (such as Mg II λ4481, the CNO blend at $\sim\lambda$4650 etc).

#91 – B1-2e (shell) – Figure 9: The Balmer lines in this spectrum are very narrow, resembling those seen in shell stars. The presence the λ4650 blend suggests an early B-type, but we lack other diagnostic lines to assign a unique type (e.g. Si III, Si IV, Mg II). With moderate signal-to-noise observations of low metallicity targets, this is a common problem in this spectral domain (c.f. star #59 above, and Evans et al. 2004). This star appears to be heavily reddened, although it is at the faint end of the photometric survey and so a relatively large degree of uncertainty in the colour can probably be expected (cf. Pietrzyński et al. 2006).

4. Stellar Radial Velocities

Radial velocities, $v_{\rm r}$, were calculated from the means of manual measurements of the line centres of absorption lines. Where possible the primary Balmer lines (Hβ, Hγ, Hδ, H8 and H9) were supplemented by measurements of He I and He II lines, and occasionally from metallic lines (e.g. in the luminous B-type supergiants). We do not use the Hϵ line owing to its blend with the Ca *H* line.

The mean $v_{\rm r}$ values for each of our targets are given in Table 2, together with 1-σ uncertainties and the number of lines used (dependent on both the spectral type of the star, and the data quality). To investigate the spatial variation of the radial velocities we initially binned our results. The median 1-σ (internal) uncertainty is 19 kms^{-1}, but we adopt a more conservative bin-size of 50 kms^{-1}(thereby also providing a reasonable number of stars per bin). In Figure 14 we show the spatial distribution of the stars in each of four bins, i.e. $v_{\rm r}< 350$, $350 < v_{\rm r}< 400$, $400 < v_{\rm r}< 450$, and $v_{\rm r}> 450$ kms^{-1}. Although limited by both sample size and velocity precision, Figure 14 shows a trend of increasing velocities with increasing right ascension, i.e. rotation of the galaxy as traced by the young stellar population.

In Figure 15 we plot differential velocities, Δv (i.e. $v_{\rm r} - v_{\rm sys}$), as a function of radius along the main disk of the galaxy, taking the systemic velocity ($v_{\rm sys}$) as 402 kms^{-1} (Blais-Ouellette et al. 2001). We have corrected the velocities in the figure for an inclination of 75$^{\rm o}$ (Jobin & Carignan 1990). The radius is calculated by finding the radial distance

of each star from the optical centre of the galaxy ($\alpha = 10^{\rm h}03^{\rm m}06\overset{\rm s}{.}6$, $\delta = -26^{\rm o}09'32''$, J2000.0; Blais-Ouellette et al. 2001), projected onto the major axis of the galaxy. The position angle of NGC 3109 is 93° (Jobin & Carignan 1990), so the projection term related to this component is relatively minor. In Figure 15 we also plot rotation curves from H I observations (Jobin & Carignan, solid line, shifted by 2 kms^{-1} so that the systemic velocities tally) and Hα (Blais-Ouellette et al., dotted line).

In general, the stars track the H I and Hα rotation curves, but with a fair degree of scatter. Further observations would be of significant value to determine whether the stellar results are revealing genuine sub-structures in the disk, or if we are simply limited by the small sample (and/or undetected nebular contamination at our relatively low spectral resolution).

5. Stellar abundances in NGC 3109

Early B-type supergiants have numerous metallic absorption lines that are useful for abundance determinations. Here we analyse eight supergiants from our sample using the FASTWIND model atmosphere code (Santolaya-Rey et al. 1997; Puls et al. 2005). The methods for quantitative analysis at the spectral resolution from FORS are described in detail elsewhere (Urbaneja et al. 2003, 2005a). In brief, each model is described by an effective temperature ($T_{\rm eff}$), a surface gravity and a stellar radius, each of which is defined at $\tau_{\rm Ross} = 2/3$. Additional model parameters are the exponent of the wind velocity law (β), the microturbulent velocity ($v_{\rm turb}$), the mass-loss rate ($\dot{M}$), the wind terminal velocity (v_∞) and a set of chemical abundances. Terminal velocities are taken from the spectral type–v_∞ relation from Kudritzki & Puls (2000).

To limit the number of free parameters, we follow the approach described by Urbaneja et al. (2005b), namely fitting the effective temperature, surface gravity, global metallicty and Q' (which, at fixed v_∞, takes into account the mass-loss rate and stellar radius). In calculation of the atmospheric structure $v_{\rm turb}$ is fixed to 10 kms^{-1}, but this is then varied in the spectral synthesis to obtain uniform abundances from different lines of the same metallic species.

The extinction and absolute magnitudes of our targets are given in Table 3. The colour excess, $E(V - I_{\rm c})$, was calculated from the observed colours (Table 2) and intrinsic colours obtained from the FASTWIND models, convolved with the appropriate filter. Some iteration

is required here, but once the stellar radius is approximately correct, the colours do not vary significantly. The V-band extinction (A_V) was found using the relations from Cardelli et al. (1989) to calculate the (Cousins) I-band extinction. Absolute magnitudes (M_V) were then calculated taking the distance modulus to NGC 3109 as 25.57 (Soszyński et al. 2006). Note that non-physical (i.e. negative) colour excesses were obtained for two of our targets (#7 and #22), likely due to nearby H II regions. For these two stars the mean extinction from Soszyński et al. (2006) of $E(B-V) = 0.09$ was adopted.

Effective temperatures, microturbulent velocities, and silicon abundances were obtained from fits to the Si II/III/IV lines, with gravities and wind mass-loss rates obtained from fits to the Balmer lines, principally Hβ. The Hα line is a better diagnostic of the stellar wind, but at the distance of NGC 3109 the nebular emission varies on very small scales and sky-subtraction becomes critical. Even with the FORS slitlets, there is evidence for over/under-subtraction in many of the Hα profiles (cf. the nebular lines), and we do not use Hα in our analysis. The associated uncertainties of this method are $T_{\rm eff} \pm$ 1,000 K and log$g\pm$ 0.1 dex (see discussion by Urbaneja et al. 2005b).

The primary abundance diagnostics for nitrogen and oxygen are: N II $\lambda\lambda$3995, 5050, 5100; O II $\lambda\lambda$4072-76, 4317-19, 4414-16. There are also many weaker lines and the optimum model is determined by attempting to reproduce as many features as possible – the results are included in Table 4. The dependence of the chemical abundances on the adopted stellar parameters is shown for two of our stars in Tables 5 and 6. The combined uncertainties from different parameters (added in quadrature) are shown in the final columns, with individual abundances robust to $\pm$0.2 dex.

We also estimate abundances for Mg II λ4481 and Si III $\lambda\lambda$4553-72. These are less secure than the nitrogen and oxygen abundances due to the smaller number of lines and their relative weakness. Moreover, we do not quote carbon abundances for our stars. The primary isolated line of carbon is C II λ4267, which is barely visible in the FORS spectra, notwithstanding the fact that there are many problems regarding the use of this line in theoretical models (e.g. Lennon et al. 2003). The rich blend of CNO lines around λ4650 can provide an indirect tracer of the carbon abundance, but from data at this spectral resolution the combined uncertainties render any value as very unreliable.

A summary of the physical parameters for the B-type supergiants is given in Table 4. The final FASTWIND models are compared with the FORS spectra in Figures 16 and 17, in which the model spectra have been smoothed to the effective resolution of the observations.

In Figures 18 and 19 we show models for stars #22 and #37 in which the metallic abundances are ±0.2 dex compared to the adopted values – in some cases individual O II lines are better fit by the increased or decreased values, but we consider the fit to multiple lines in our determination of the final abundance.

The mean oxygen abundance is 12 + log(O/H) = 7.76 ±0.07 (1-sigma systematic uncertainty). This is in excellent agreement with results from H II regions. Lee et al. (2003b) give an oxygen abundance of 7.73 for one target, and Lee et al. (2003a) found a mean of 7.63 for a further five regions. Moreover, new results from ∼10 compact H II regions find a mean abundance of 7.74 ± 0.10 (Dr. M. Peña, private communication). The mean oxygen abundance found here is also comparable to recent results for stars in the WLM galaxy (Bresolin et al. 2006). We note that oxygen abundances are typically considered in 0.1 dex increments between models, so the mean values here give the impression of unrealistic precision. The median value for our 8 stars is 7.8 (cf. 7.9 from the three stars in WLM). The results are significantly lower than those found for stars in the SMC, for which log(O/H)+12 = 8.13 and 8.14 for B- and A-type supergiants respectively (Trundle et al. 2004; Trundle & Lennon 2005; Venn 1999).

Our abundance estimates for magnesium and silicon are more in keeping with those found in the SMC stars from Trundle & Lennon (2005). However, in many cases our estimates are upper limits, and the exact abundance of the alpha-elements will require higher-resolution spectroscopy.

Where of note, we now provide brief comments on specific stars:

#11: The O II feature at $\lambda\lambda$4072-76 is somewhat distorted, with some uncertainty in definition of the continuum. Only upper limits are possible for both nitrogen and magnesium as there are not significant lines from either element. The mass-loss rate was fixed to reproduce Hβ, with $T_{\rm eff}$ from the ionization balance of He I/II and Si III/IV.

#7: The spectrum of #7 suffers from significant emission from a nearby H II region. Both Hα and Hβ are strongly contaminated, with Hγ and Hδ also in-filled somewhat. The gravity for this star was obtained from the higher-order Balmer lines, that appear well reproduced. $T_{\rm eff}$ was found from the balance of He I/II and Si III/IV. Again the nitrogen abundance is an upper limit.

#9: The mass-loss rate was fixed to reproduce Hβ, although the line-core is not well matched – Hα shows some nebular contamination, it is likely that Hβ is also infilled slightly.

#22: The strong absorption close to λ3995 is not consistent with being from N II when the other nitrogen features in this spectrum are considered – the observed absorption is also very slightly red-shifted and its origins remain unclear.

#37: The ionization balance of Si II/III/IV is used to find $T_{\rm eff}$ – note that this star is a 'transitional' type in which neither the Si II nor the Si IV lines are strong.

6. NGC 3109 as a target for future extremely large telescopes

Plans for the next generation of large ground-based telescopes (the so-called extremely large telescopes, or ELTs) are now gaining momentum. Excluding the big spiral galaxies, the total stellar mass in NGC 3109 is larger than in other Local Group systems – in the context of ELTs, NGC 3109 presents an exciting opportunity to study many stages of stellar evolution in a very metal-poor environment. With a 30-m primary aperture, good signal-to-noise spectra could be obtained down to approximately $M_V = -2$. Such observations would enable detailed studies of the young, massive population (i.e. O- and early B-type stars on the main-sequence) and of stars on the asymptotic giant branch (AGB). The fainter stars could be observed at spectral resolutions comparable to those from FORS, with higher resolutions ($R \sim 20{,}000$) employed to investigate wind parameters and abundances in, for example, main-sequence O-type stars.

Moreover, with less demanding signal-to-noise requirements, an ELT would be able to trace the kinematics of the non-supergiant population (via e.g. the calcium triplet). Crucial input to cosmological simulations could be obtained from observations along the major and minor axes of NGC 3109, to fully investigate the structure of this dark-matter dominated dwarf.

We also note that most of the current plans for ELT instruments include some degree of adaptive optics (AO) correction (e.g. Cunningham et al. 2006). For observations in NGC 3109, a 'seeing-limited' optical instrument should be adequate, e.g. the Wide Field Optical Spectrograph (WFOS) proposed for the Thirty Meter Telescope (TMT) project (e.g. Pazder et al. 2006). However, at larger distances and finer spatial scales, the AO systems will most likely restrict observers to near-IR wavelengths. Quantitative studies of OB-type stars in this domain have advanced in recent years (e.g. Lenorzer et al. 2004; Repolust et al. 2005; Hanson et al. 2005). To fully exploit the likely capabilities of an ELT, continued efforts are required in this region – both in terms of atomic data (e.g. Przybilla

2005), and comparison studies in the Milky Way and Magellanic Clouds.

7. Summary

We have presented spectra from an exploratory survey of the young, massive-star content of NGC 3109. These are the first spectral observations of the young stellar population in this galaxy. Although of limited resolving power, the spectra have been used to estimate stellar radial velocities, which appear largely consistent with published rotation curves from observations of the gas. Our stellar oxygen abundances agree with recent results from H II regions, and are significantly lower than those found for stars in the SMC (e.g. Trundle & Lennon 2005). They are also comparable to those in the WLM galaxy (Bresolin et al. 2006). We require higher-resolution spectroscopy to obtain precise abundances for the alpha-elements, but it is clear that the stars in NGC 3109 have metal abundances that are very deficient when compared to the solar neighbourhood, and likely even lower than in the SMC.

8. Acknowledgements

CJE acknowledges financial support from the UK Particle Physics and Astronomy Research Council (PPARC). GP and WG gratefully acknowledge financial support for this work from the Chilean Center for Astrophysics, under grant FONDAP 15010003. We thank the referee for their constructive comments.

REFERENCES

Asplund, M., Grevesse, N., & Sauval, A. J. 2005, in Cosmic Abundances as Records of Stellar Evolution and Nucleosynthesis, ed. T. G. Barnes III & F. N. Bash (ASP Conference Series vol. 336, San Francisco), 25

Barnes, D. G. & de Blok, W. J. G. 2001, AJ, 122, 825

Blais-Ouellette, S., Amram, P., & Carignan, C. 2001, AJ, 121, 1952

Bresolin, F., Capaccioli, M., & Piotto, G. 1993, AJ, 105, 1779

Bresolin, F., Pietrzyński, G., Urbaneja, M. A., et al. 2006, ApJ, 648, 1007

Burstein, D. & Heiles, C. 1984, ApJS, 54, 33

Capaccioli, M., Piotto, G., & Bresolin, F. 1992, AJ, 103, 1151

Cardelli, J. A., Clayton, G. C., & Mathis, J. S. 1989, ApJ, 345, 245

Cunningham, C., Atad-Ettadgui, E., Bacon, R., et al. 2006, in Ground-based and Airborne Instrumentation for Astronomy, ed. I. S. McLean & M. Iye, Vol. 6269 (Proceedings of the SPIE), p58

Davidge, T. J. 1993, AJ, 105, 1392

de Vaucouleurs, G., de Vaucouleurs, A., Corwin, H. G., et al. 1991, Third Reference Catalogue of Bright Galaxies (Springer-Verlag, New York)

Demers, S., Battinelli, P., & Letarte, B. 2003, A&A, 410, 795

Demers, S., Kunkel, W. E., & Irwin, M. J. 1985, AJ, 90, 1967

Elias, J. H. & Frogel, J. A. 1985, ApJ, 289, 141

Evans, C. J. & Howarth, I. D. 2003, MNRAS, 345, 1223

Evans, C. J., Howarth, I. D., Irwin, M. J., Burnley, A. W., & Harries, T. J. 2004, MNRAS, 353, 601

Greggio, L., Marconi, G., Tosi, M., & Focardi, P. 1993, AJ, 105, 894

Hanson, M. M., Kudritzki, R.-P., Kenworthy, M. A., Puls, J., & Tokunaga, A. T. 2005, ApJS, 161, 154

Jobin, M. & Carignan, C. 1990, AJ, 100, 648

Kudritzki, R.-P. & Puls, J. 2000, ARA&A, 38, 613

Lake, G. 1989, ApJ, 345, L17

Lee, H., Grebel, E. K., & Hodge, P. W. 2003a, A&A, 401, 141

Lee, H., McCall, M. L., Kingsburgh, R. L., Ross, R., & Stevenson, C. C. 2003b, AJ, 125, 146

Lee, M. G. 1993, ApJ, 408, 409

Lennon, D. J. 1997, A&A, 317, 871

Lennon, D. J., Dufton, P. L., & Crowley, C. 2003, A&A, 398, 455

Lenorzer, A., Mokiem, M. R., de Koter, A., & Puls, J. 2004, A&A, 422, 275

Milgrom, M. 1983, ApJ, 270, 365

Milgrom, M. 1991, ApJ, 367, 490

Minniti, D., Zijlstra, A. A., & Alonso, M. V. 1999, AJ, 117, 881

Navarro, J. F., Frenk, C. S., & White, S. D. M. 1996, ApJ, 462, 563

Pazder, J., Fletcher, M., & Morbey, C. 2006, in Ground-based and Airborne Instrumentation for Astronomy, ed. I. S. McLean & M. Iye, Vol. 6269 (Proceedings of the SPIE), p97

Pietrzyński, G., Gieren, W., Udalski, A., et al. 2006, ApJ, 648, 366

Przybilla, N. 2005, A&A, 443, 293

Puls, J., Urbaneja, M. A., Venero, R., et al. 2005, A&A, 435, 669

Repolust, T., Puls, J., Hanson, M. M., Kudritzki, R.-P., & Mokiem, M. R. 2005, A&A, 440, 261

Sandage, A. & Carlson, G. 1988, AJ, 95, 1599

Santolaya-Rey, A. E., Puls, J., & Herrero, A. 1997, A&A, 323, 488

Soszyński, I., Gieren, W., Pietrzyński, G., et al. 2006, ApJ, 648, 375

Trundle, C. & Lennon, D. J. 2005, A&A, 434, 677

Trundle, C., Lennon, D. J., Puls, J., & Dufton, P. L. 2004, A&A, 417, 217

Urbaneja, M. A., Herrero, A., Bresolin, F., et al. 2003, ApJ, 584, 73

Urbaneja, M. A., Herrero, A., Bresolin, F., et al. 2005a, ApJ, 622, 862

Urbaneja, M. A., Herrero, A., Kudritzki, R.-P., et al. 2005b, ApJ, 635, 311

Valenzuela, O., Rhee, G., Klypin, A., et al. 2006, ApJ, astro-ph/0509644

van Dokkum, P. G. 2001, PASP, 113, 1420

Venn, K. A. 1999, ApJ, 518, 405

Walborn, N. R. & Fitzpatrick, E. L. 1990, PASP, 102, 379

Walborn, N. R., Lennon, D. J., Heap, S. R., et al. 2000, PASP, 112, 1243

Table 1. Summary of observations

Field	Grism	Date	Exposure time [sec]
1	600B	2004-02-24	4×2700
2	600B	2004-02-25	4×2400
3	600B	2004-02-24	3×2700+1×2400
4	600B	2004-02-25	1×2700+2×2400
1	1200R	2004-02-24	4×2500
2	1200R	2004-02-25	4×2400

Table 2. Observational parameters of target stars

Star	Field	α (J2000.0)	δ (J2000.0)	V	$V-I_c$	Spectral Type	v_r (kms^{-1})	σ (kms^{-1})	# lines	S/N	Comment
1	2	10 03 11.93	−26 09 29.01	17.81	0.28	A2 Ia	412	9	5	195	
2	1	10 03 27.47	−26 10 06.41	18.05	0.17	mid Be	477	9	6	180	SC88-B155
3	1	10 03 17.66	−26 10 00.67	18.07	−0.06	B1 Ia	419	24	9	110	SC88-B80
4	2	10 03 16.74	−26 09 22.90	18.36	0.14	B9 Ia	454	25	8	100	SC88-B75
5	2	10 03 05.37	−26 08 56.58	18.54	0.05	B8 Ia	411	23	10	95	SC88-B56
6	2	10 02 52.99	−26 09 51.65	18.62	0.05	B8 Ia	370	8	10	140	SC88-B34
7	2	10 02 54.69	−26 08 59.64	18.69	−0.26	B0-1 Ia	382	19	10	110	SC88-B138
8	3	10 02 53.15	−26 09 37.03	18.76	0.30	A7 II	393	19	5	95	SC88-B36
9	2	10 02 49.77	−26 08 45.04	18.78	−0.20	B0.5 Ia	375	16	9	140	SC88-B136
10	1	10 03 26.63	−26 08 54.24	18.80	0.08	B: +em/neb?	464	20	5	65	SC88-B120
11	1	10 02 58.61	−26 09 50.95	18.91	−0.08	B0 I	354	22	7	125	SC88-B148
12	1	10 03 07.09	−26 09 41.26	18.92	0.11	B8 Ia	399	15	7	80	SC88-B57
13	2	10 03 08.51	−26 09 57.31	19.02	0.16	A0 Iab	405	12	5	130	SC88-B67
14	2	10 02 59.54	−26 09 12.44	19.03	1.71	G2 I	317	18	3	–	SC88-R14
15	2	10 03 13.10	−26 09 35.61	19.04	−0.01	B5 Ia	419	17	12	120	SC88-B90
16	2	10 03 10.06	−26 09 48.53	19.05	0.35	A7 II	381	17	5	60	
17	1	10 03 20.21	−26 06 44.62	19.17	0.26	A3 II	447	23	5	50	DKI1874
18	2	10 02 57.76	−26 08 33.25	19.21	0.19	B1 I	392	29	6	105	SC88-B104
19	3	10 02 49.67	−26 09 21.95	19.32	−0.15	B1 Ia	363	17	11	85	SC88-B33
20	2	10 03 03.22	−26 09 21.41	19.33	−0.14	O8 I	407	11	8	70	
21	3	10 03 09.96	−26 08 27.11	19.33	0.15	A0 Iab	397	20	5	50	
22	2	10 02 59.88	−26 09 12.60	19.36	−0.21	B1 Ia	391	25	14	65	
23	1	10 03 19.95	−26 09 55.01	19.44	0.14	A1 Ib	453	18	5	130	SC88-V14a
24	1	10 03 01.89	−26 09 01.04	19.46	−0.01	B2-3 Iab	346	15	11	80	
25	1	10 03 22.95	−26 10 30.91	19.47	0.11	A0 Ib	429	7	5	90	
26	2	10 02 46.32	−26 09 46.88	19.48	−0.19	B3 Ib	337	13	11	140	
27	2	10 03 01.85	−26 09 08.91	19.49	0.00	B2.5 Ia	420	17	10	90	
28	1	10 03 08.51	−26 09 21.56	19.51	0.05	B2.5 Iab	390	30	11	90	
29	1	10 03 12.50	−26 10 14.81	19.54	0.02	B8 Ia	421	13	8	75	
30	2	10 02 55.53	−26 09 54.82	19.54	−0.01	A0 Iab	400	21	7	85	
31	3	10 02 55.55	−26 10 03.57	19.54	−0.16	B1-2 Ib	409	34	10	60	
32	1	10 03 03.41	−26 08 46.06	19.57	0.25	A3 II	370	8	5	95	SC88-V7,65a
33	3	10 03 02.45	−26 09 36.11	19.57	−0.18	O9 If	334	33	5	60	
34	1	10 03 14.24	−26 09 16.96	19.61	−0.25	O8 I(f)	409	25	10	90	
35	3	10 03 13.65	−26 09 55.76	19.70	−0.15	O8-9.5 I(f)	476	16	7	60	
36	1	10 03 29.56	−26 08 39.96	19.71	0.19	mid B	–	–	–	80	P Cyg em.
37	2	10 02 47.33	−26 09 45.07	19.73	−0.11	B2 Iab	364	22	13	90	
38	2	10 02 56.57	−26 09 55.58	19.77	0.16	B1-3 III	379	30	8	50	
39	4	10 02 46.97	−26 10 14.34	19.79	−0.17	O9.5 II:	337	33	6	70	
40	2	10 03 14.72	−26 09 57.40	19.81	−0.05	B8 Ib	430	13	5	90	
41	3	10 03 11.85	−26 10 08.64	19.81	0.05	A0 Iab	454	28	4	55	
42	3	10 03 01.36	−26 08 26.69	19.86	−0.24	B0-2	428	22	5	55	

Table 2—Continued

Star	Field	α (J2000.0)	δ (J2000.0)	V	$V-I_c$	Spectral Type	v_r (kms^{-1})	σ (kms^{-1})	# lines	S/N	Comment
43	4	10 03 11.73	−26 10 18.00	19.94	−0.19	O9.5 I	424	24	6	40	
44	3	10 02 58.59	−26 09 58.04	19.95	−0.08	early-B Ib	394	33	7	35	
45	4	10 03 16.55	−26 09 38.46	19.97	0.10	B8-A0 I	441	20	5	25	
46	4	10 02 55.61	−26 08 58.35	19.98	−0.31	early-B	394	15	9	40	
47	3	10 02 55.09	−26 10 07.25	19.99	−0.12	B2.5 Ib	408	28	6	65	
48	4	10 02 56.20	−26 08 58.23	19.99	−0.19	late-O If	–	–	–	40	str. HII
49	3	10 02 59.69	−26 09 24.38	20.00	−0.22	O9 II	390	29	5	40	
50	1	10 03 10.62	−26 09 22.56	20.05	−0.02	B8: Ib	399	10	3	80	
51	4	10 02 54.45	−26 09 03.69	20.05	−0.26	early-B (B0?)	351	20	5	60	
52	3	10 02 51.78	−26 09 42.14	20.07	0.03	A0 Ib	381	22	5	45	
53	4	10 02 51.40	−26 09 35.02	20.07	−0.16	B0: Ib	405	35	5	55	
54	3	10 02 46.61	−26 09 12.45	20.10	−0.18	B1-3 II-Ib	352	23	5	45	
55	4	10 03 04.04	−26 09 10.30	20.12	−0.35	B0-2	413	19	6	45	str. HII at Hβ
56	4	10 02 46.16	−26 09 55.26	20.14	−0.17	early-B	–	–	–	65	
57	4	10 02 47.12	−26 10 14.27	20.15	−0.33	early-B	372	22	6	45	
58	4	10 02 53.27	−26 09 48.92	20.17	−0.13	B9: Iab	385	10	5	35	
59	1	10 03 15.31	−26 09 24.64	20.21	−0.19	B0-3	446	15	10	75	
60	3	10 03 08.17	−26 10 18.11	20.22	−0.17	B0-0.5	434	31	8	35	
61	3	10 03 16.54	−26 10 20.96	20.23	−0.11	early-B?	–	–	–	60	str. HII
62	3	10 03 14.60	−26 10 06.00	20.24	0.18	A5 II	475	19	5	50	SC88-V9,45,57a
63	1	10 03 00.10	−26 09 28.72	20.25	−0.42	late-O	–	–	–	55	str. HII
64	2	10 02 51.43	−26 08 47.06	20.25	−0.03	B0-2	565	23	8	55	
65	4	10 03 13.39	−26 08 03.31	20.26	−0.19	early-B	490	16	4	35	shell star?
66	4	10 03 01.39	−26 08 01.48	20.29	0.06	late-O	–	–	–	40	str. HII
67	1	10 03 24.64	−26 09 35.03	20.31	0.34	A5 II	454	11	5	50	
68	4	10 03 02.57	−26 09 30.70	20.33	0.00	A0 Iab:	412	15	5	30	
69	4	10 03 07.76	−26 09 17.48	20.36	−0.13	early-mid B	408	33	6	30	
70	4	10 02 58.97	−26 08 11.58	20.36	−0.30	B5 Ia	424	33	5	40	SC88-V6,25,31a
71	4	10 03 14.15	−26 10 06.71	20.37	0.17	B9-A0 Ib:	405	30	4	35	
72	4	10 02 49.73	−26 09 42.95	20.40	0.03	A0 Ib:	394	29	5	40	
73	4	10 02 57.30	−26 09 50.10	20.43	0.03	A0: Iab	392	11	5	35	
74	3	10 03 05.77	−26 09 11.36	20.44	–	B0-2 II:	440	17	5	40	
75	2	10 03 14.34	−26 09 57.82	20.49	0.69	F2 I	504	12	4	–	
76	4	10 03 09.41	−26 09 49.43	20.51	0.39	B9-A0 Ib	370	23	4	35	
77	3	10 03 05.03	−26 09 23.78	20.52	–	late-O	–	–	–	40	str. HII
78	2	10 02 49.47	−26 08 45.18	20.54	−0.24	O9.5 III	402	25	9	70	
79	2	10 03 05.83	−26 09 06.92	20.55	–	B9 Ib	407	11	4	40	
80	1	10 03 12.06	−26 10 14.97	20.70	−0.11	early-B (B1-2)	398	18	8	40	
81	2	10 02 47.00	−26 09 45.21	20.75	−0.16	B1: Ib	389	19	10	65	
82	3	10 03 10.90	−26 10 08.34	20.81	0.58	F2: I	382	13	3	–	
83	2	10 03 05.00	−26 08 56.13	20.85	0.32	A3 II	296	17	5	45	
84	2	10 03 02.43	−26 09 21.49	20.95	0.36	A5 II	393	27	5	30	

Table 2—Continued

Star	Field	α (J2000.0)	δ (J2000.0)	V	$V-I_c$	Spectral Type	v_r (kms^{-1})	σ (kms^{-1})	# lines	S/N	Comment
85	4	10 03 05.67	−26 09 21.20	20.98	0.46	early-B	408	33	4	25	
86	2	10 02 46.72	−26 09 47.27	21.15	0.02	late-B II	445	12	3	35	
87	3	10 03 07.81	−26 10 17.77	21.32	0.11	B	292	30	3	20	SC88-V36c
88	1	10 03 05.60	−26 09 17.03	21.41	–	early-mid B	455	14	5	30	
89	1	10 03 00.81	−26 09 28.20	21.68	0.52	A5: II	263	22	4	20	
90	2	10 02 59.31	−26 09 12.72	21.73	0.31	A7 II:	482	14	3	25	
91	1	10 03 27.18	−26 10 06.11	22.22	1.21	B1-2e (shell)	440	18	9	55	

References. — DKI (Demers et al. 1985); SC88 (Sandage & Carlson 1988)

Table 3. Extinction and absolute magnitudes for target stars

ID	Sp. Type	V	$V-I_c$	E$(V-I_c)$	A$_V$	$E(B-V)$	M$_V$
11	B0 I	18.91	−0.08	0.16	0.41	0.13	−7.07
7	B0-1 Ia	18.69	−0.26	−0.04	0.27	0.09	−7.15
9	B0.5 Ia	18.78	−0.20	0.01	0.03	0.00	−6.82
3	B1 Ia	18.07	−0.06	0.10	0.26	0.08	−7.76
22	B1 Ia	19.36	−0.21	−0.02	0.27	0.09	−6.48
37	B2 Iab	19.73	−0.11	0.04	0.10	0.03	−5.94
27	B2.5 Ia	19.49	0.00	0.15	0.39	0.13	−6.47
28	B2.5 Iab	19.51	0.05	0.20	0.52	0.17	−6.58

Note. — The observed colour excesses for stars #7 and #22 are non-physical, due to likely contamination by nearby H II regions. The adopted $E(B-V)$ is the mean from Soszyński et al. (2006)

Table 4. Physical parameters of target stars

ID	Sp. Type	$T_{\rm eff}$ [kK]	log$g$	R [$R_\odot$]	$M_{\rm spec}$ [$M_\odot$]	log($L/L_\odot$)	$v_{\rm turb}$ [kms^{-1}]	$Y_{\rm He}$	$\epsilon_{\rm N}$	$\epsilon_{\rm O}$	$\epsilon_{\rm Mg}$	$\epsilon_{\rm Si}$	[O/H] [dex]
11	B0 I	27.5	3.05	35.5	51.6	5.81	12	0.10	<7.3	7.8	6.9	6.7	−0.9
7	B0-1 Ia	27.0	2.90	37.0	39.7	5.82	12	0.10	<7.5	7.8	7.0	6.9	−0.9
9	B0.5 Ia	25.0	2.75	34.5	24.4	5.62	12	0.10	7.7	7.8	7.0	7.0	−0.9
3	B1 Ia	23.5	2.50	56.2	36.5	5.94	15	0.10	7.4	7.7	6.8	6.8	−1.0
22	B1 Ia	22.0	2.60	33.0	15.6	5.35	15	0.15	7.7	7.8	6.9	6.9	−0.9
37	B2 Iab	20.5	2.70	28.0	14.3	5.04	10	0.15	7.3	7.6	6.9	6.9	−1.1
27	B2.5 Ia	19.0	2.40	37.0	12.5	5.20	12	0.13	7.7	7.8	7.1	7.0	−0.9
28	B2.5 Iab	19.0	2.55	39.0	19.7	5.25	10	0.10	7.7	7.8	7.1	7.1	−0.9

Note. — $\epsilon_{\rm X}$ = log(X/H)+12

Note. — The ratio in the final column adopts a solar abundance of $\epsilon_{\rm O}$ = 8.66 from Asplund et al. (2005)

Table 5. Abundance uncertainties as a function of stellar parameters for star #22

Element	Upper limit[a]	Lower limit[b]	$v_{\rm turb}$ [-5 kms^{-1}]	ΔHe [+0.2 dex]	ΔHe [-0.2 dex]	ΔZ [+0.2 dex]	$\Delta \log Q$ [+0.2 dex]	σ [c]
N	-0.10	-0.01	-0.08	-0.06	-0.03	-0.06	-0.06	0.16
O	-0.02	-0.08	-0.08	-0.08	-0.03	-0.05	-0.05	0.16
Mg	-0.09	0.00	-0.08	-0.05	-0.05	-0.05	-0.06	0.16
Si	-0.04	-0.01	-0.09	-0.07	0.03	-0.03	-0.06	0.14

Note. —
[a] $T_{\rm eff}$ + 1,000 K; log$g$ + 0.1 dex
[b] $T_{\rm eff}$ − 1,000 K; log$g$ − 0.1 dex
[c] The global abundance uncertainty (σ) is obtained as the square root of the sum of the squares of the uncertainties.

Table 6. Abundance uncertainties as a function of stellar parameters for star #37

Element	Upper limit[a]	Lower limit[b]	$v_{\rm turb}$ [-5 kms^{-1}]	ΔHe [+0.2 dex]	ΔHe [-0.2 dex]	ΔZ [+0.2 dex]	$\Delta \log Q$ [+0.2 dex]	σ [c]
N	-0.05	-0.08	-0.09	-0.08	-0.02	-0.05	-0.05	0.17
O	0.04	-0.14	-0.09	-0.09	-0.01	-0.03	-0.05	0.20
Mg	-0.10	0.05	-0.11	-0.04	-0.02	-0.03	-0.03	0.16
Si	0.08	-0.13	-0.13	-0.08	0.04	0.00	-0.04	0.22

Note. —
[a] $T_{\rm eff}$ + 1,000 K; log$g$ + 0.1 dex
[b] $T_{\rm eff}$ − 1,000 K; log$g$ − 0.1 dex
[c] The global abundance uncertainty (σ) is obtained as the square root of the sum of the squares of the uncertainties.

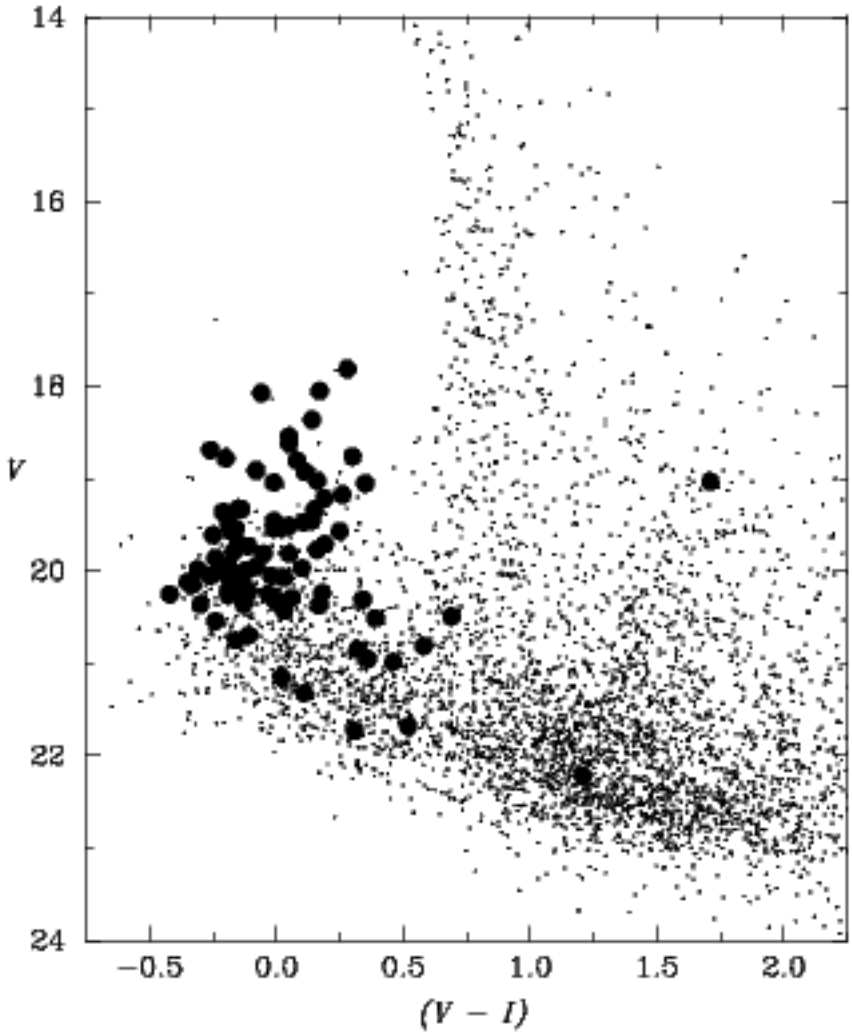

Fig. 1.— Colour-magnitude diagram of VLT-FORS targets in NGC 3109 (large closed circles), selected from V and I-band photometry (Pietrzyński et al. 2006).

Fig. 2.— FORS V-band pre-imaging of NGC 3109, with our spectroscopic targets encircled. North is at the top, east to the left. For reference the three saturated stars at the south-west of the frame are those just south of the 'F2' label in Figure 1 of Bresolin et al. (1993). The image is roughly $4\farcm0$ squared.

Fig. 3.— Target stars in NGC 3109, moving eastwards from Figure 2.

Fig. 4.— Target stars in NGC 3109, moving eastwards from Figure 3. To include #17 the image shown here is approximately $3\farcm0 \times 5\farcm0$.

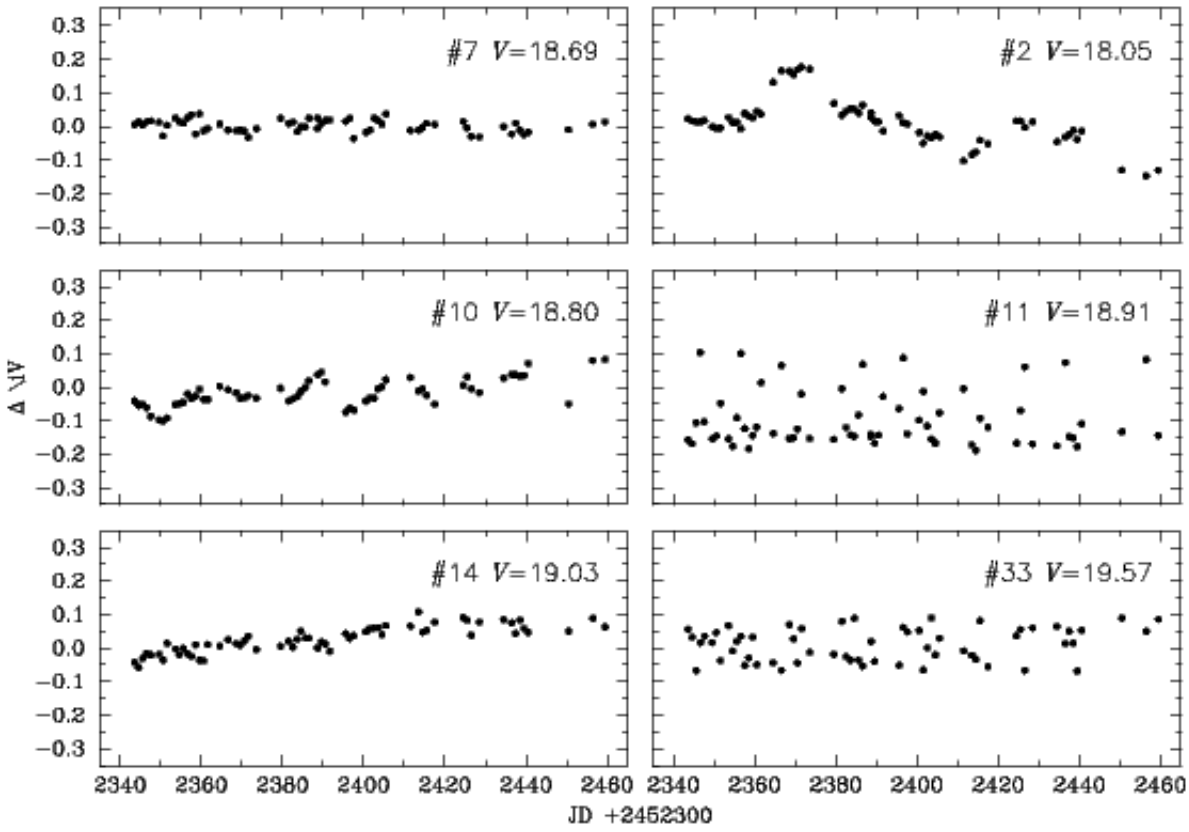

Fig. 5.— Photometric variables in NGC 3109. Star #7 is included to illustrate the scatter for a non-variable target.

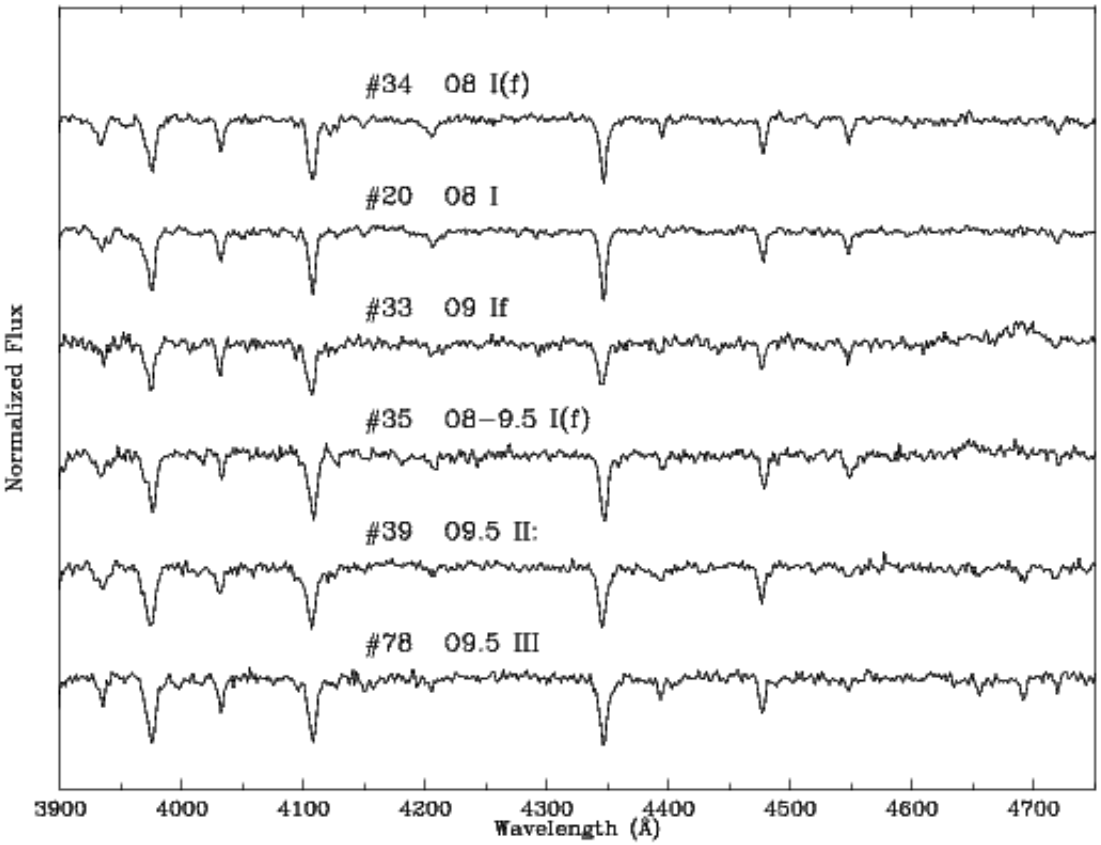

Fig. 6.— Normalized spectra of O-type stars in NGC 3109.

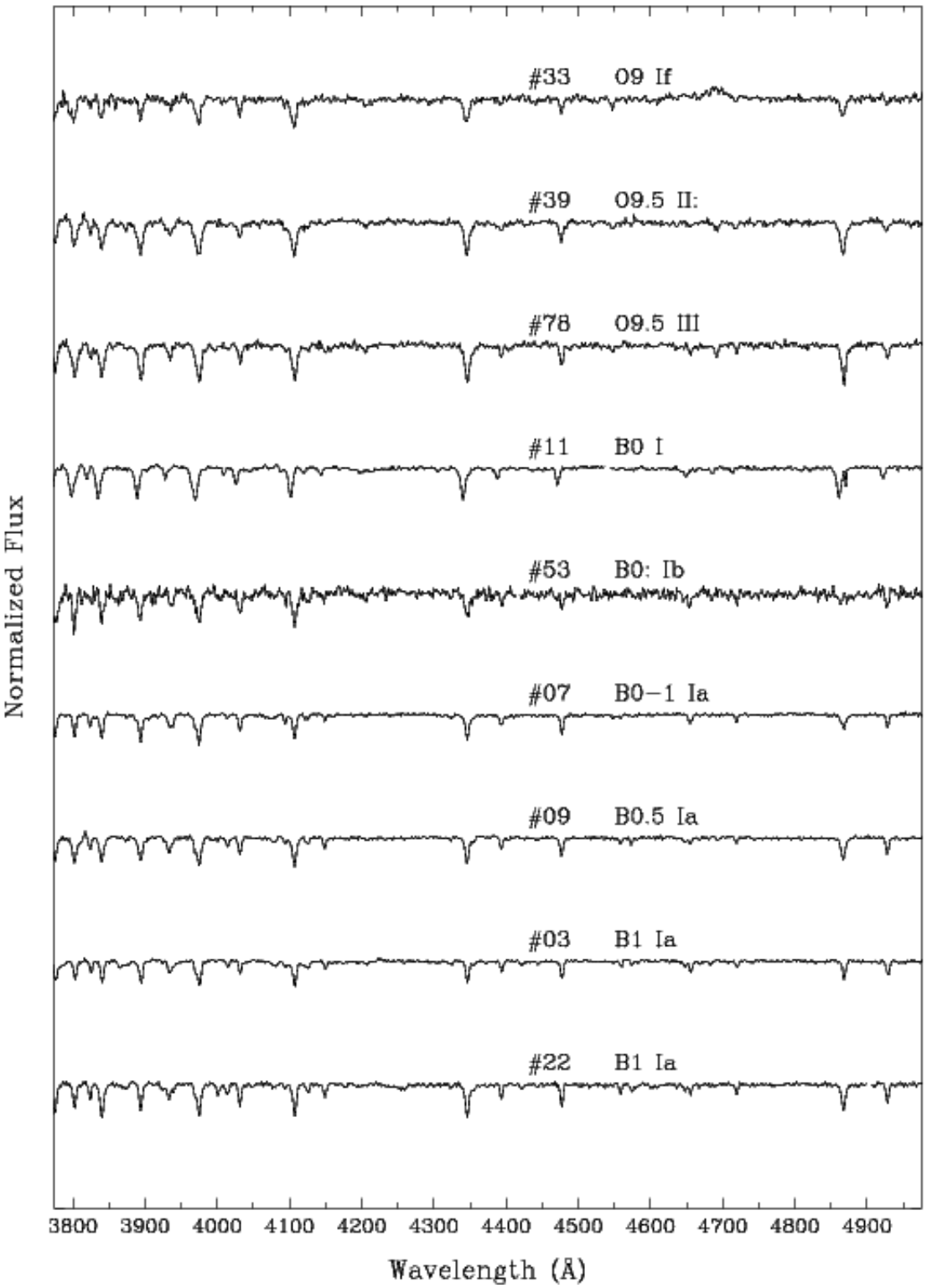

Fig. 7.— Normalized spectra of stars classified in the range O9 to B1.

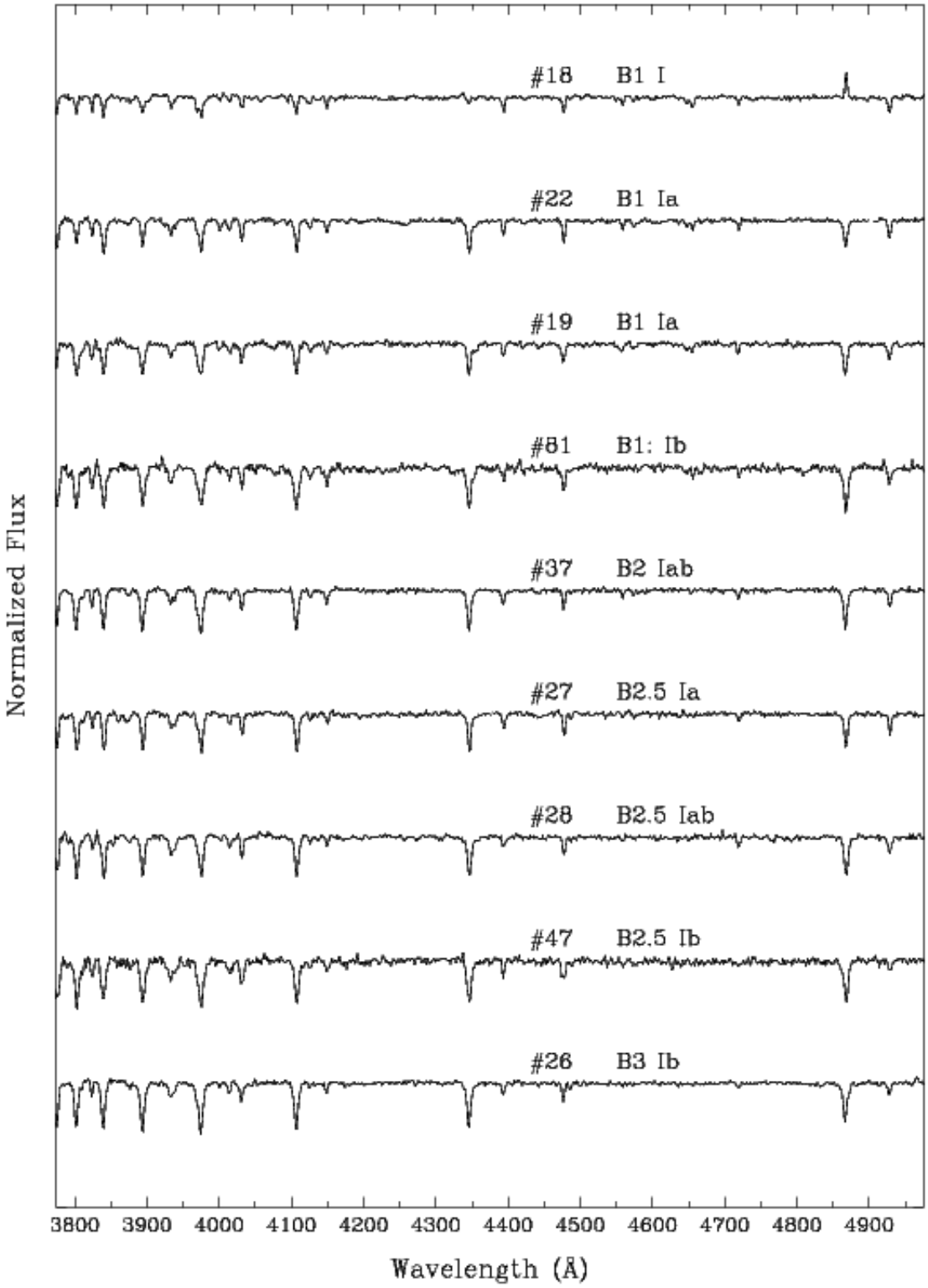

Fig. 8.— Normalized spectra of early B-type supergiants.

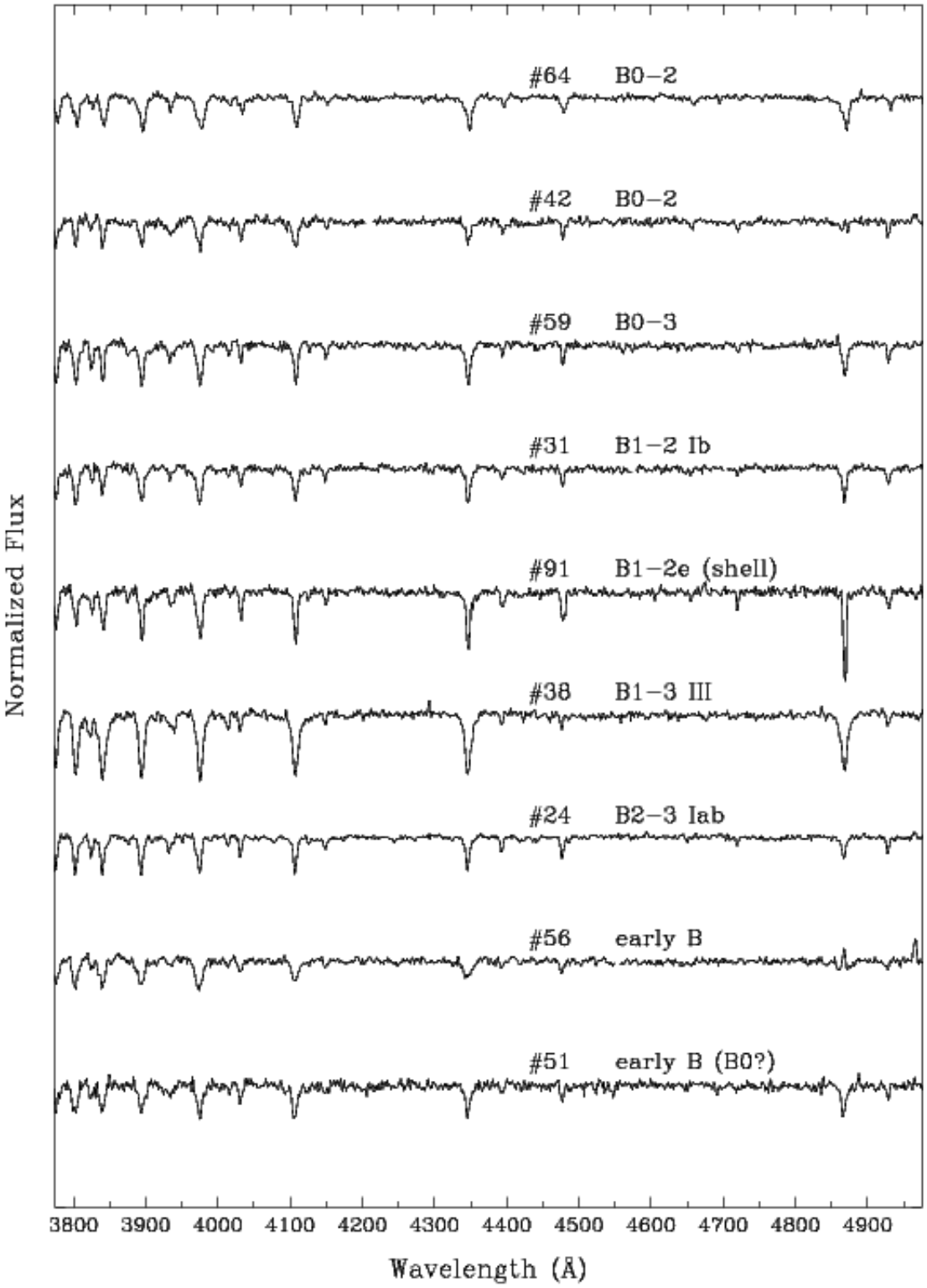

Fig. 9.— Normalized spectra of early B-type supergiants with non-unique classifications.

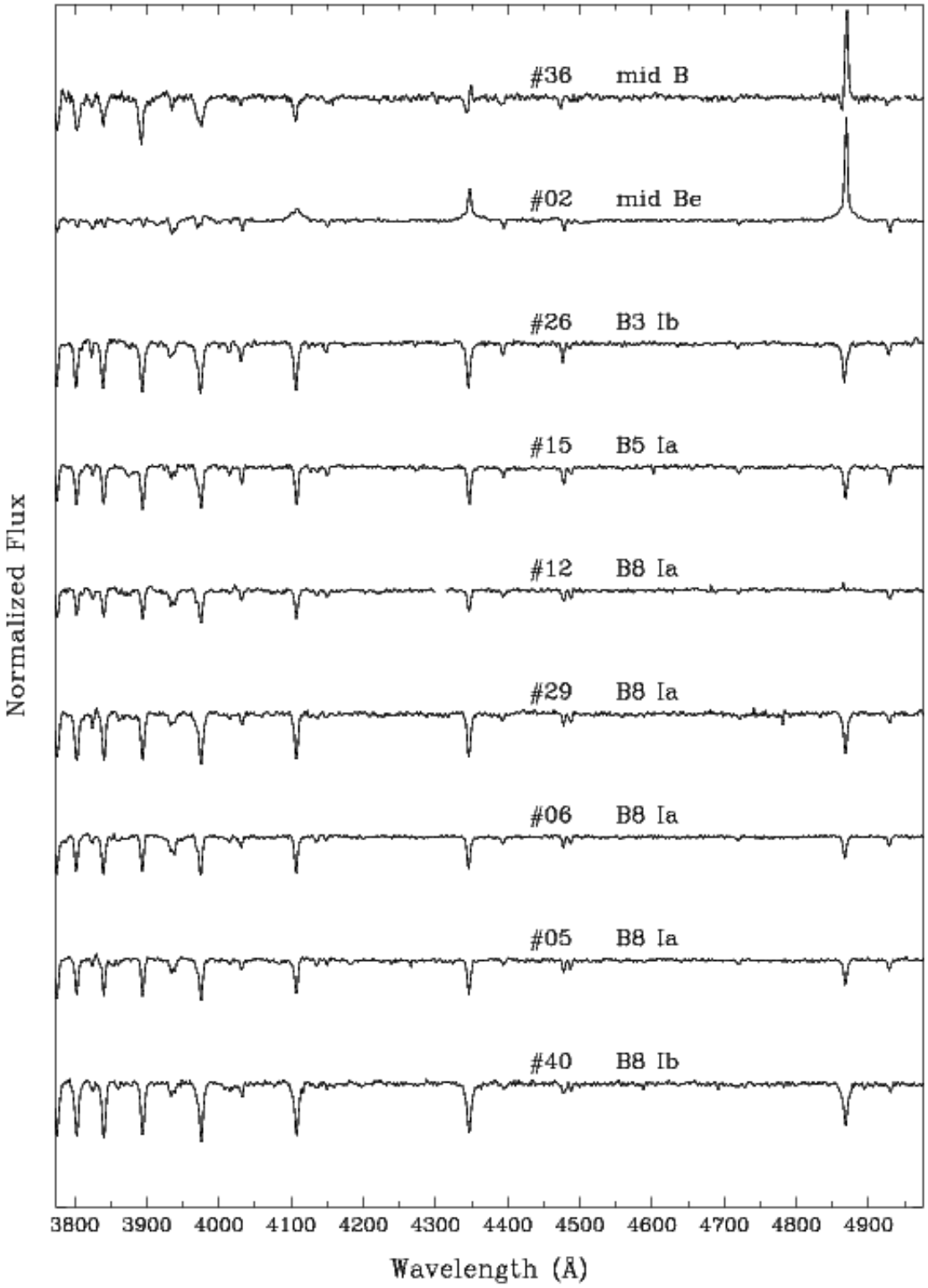

Fig. 10.— Normalized spectra of mid B-type supergiants.

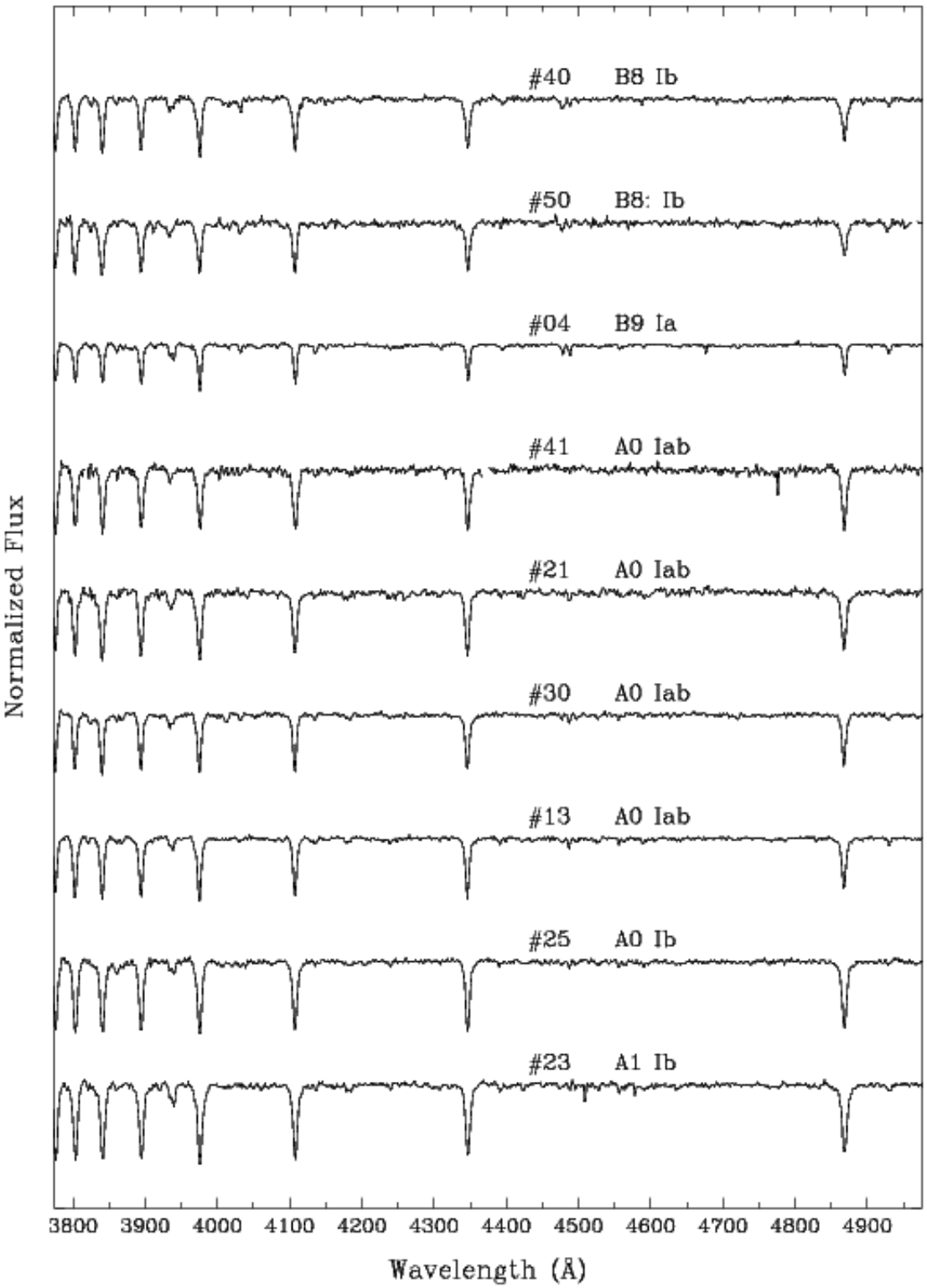

Fig. 11.— Normalized spectra of late B- and A0-type supergiants.

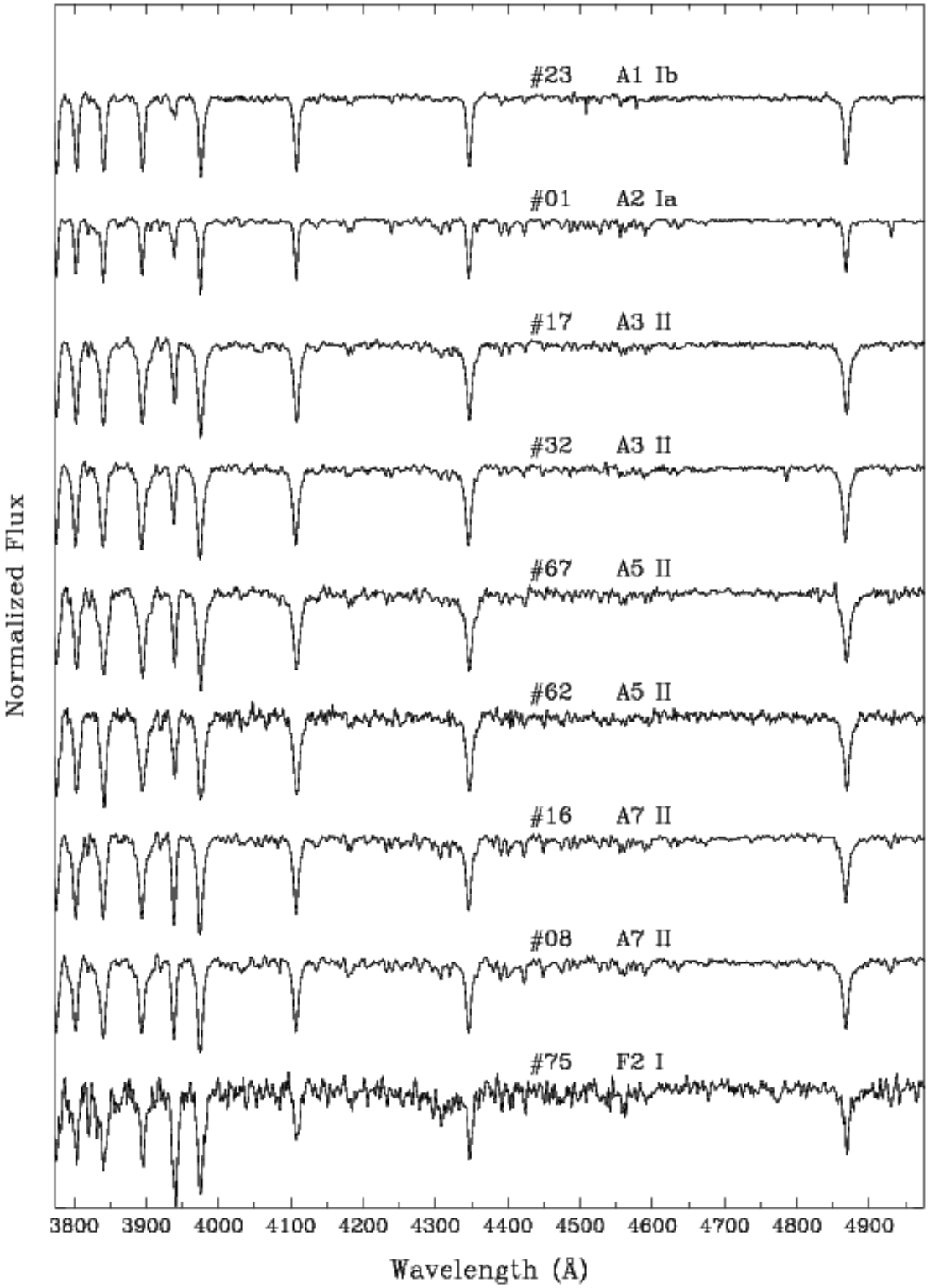

Fig. 12.— Normalized spectra of A-type supergiants and bright giants.

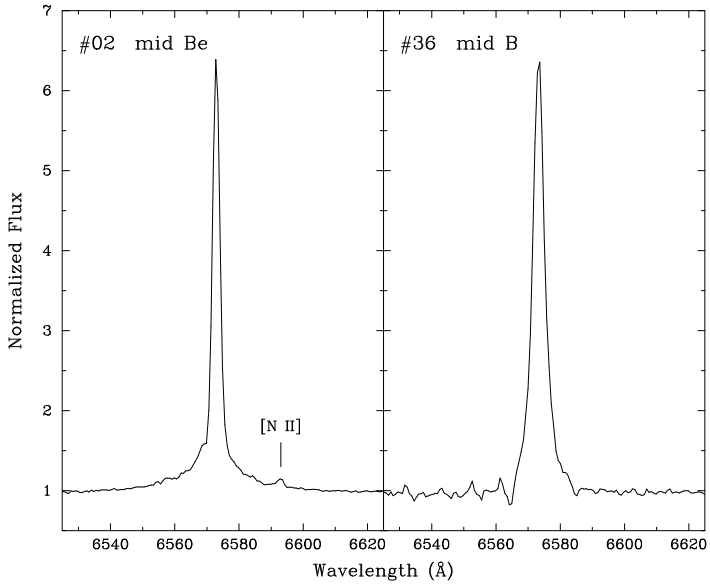

Fig. 13.— Hα spectra of two stars with significant emission profiles (>20 Å). The redshifted [N II] emission at λ6583 is the small 'bump' redward of Hα in the spectrum of #02.

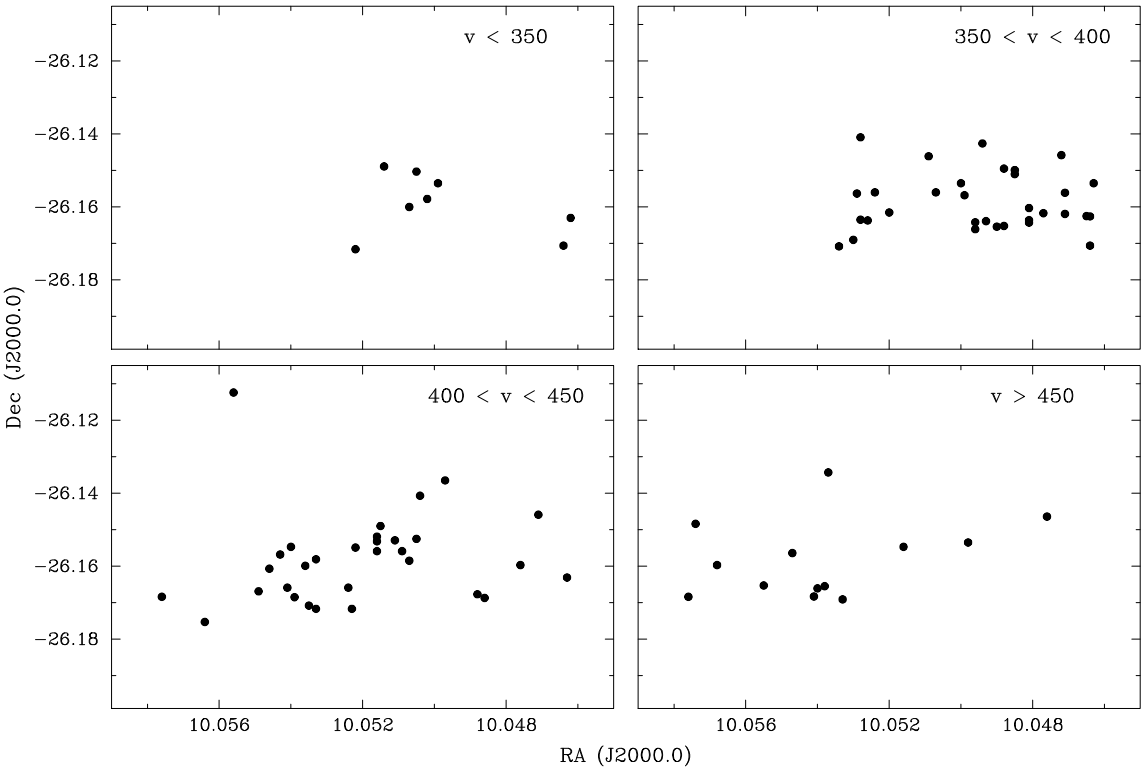

Fig. 14.— Spatial distribution of NGC 3109 targets in different radial velocity bins (in kms^{-1}), indicating a velocity gradient in the kinematics of the young stellar population across the observed region.

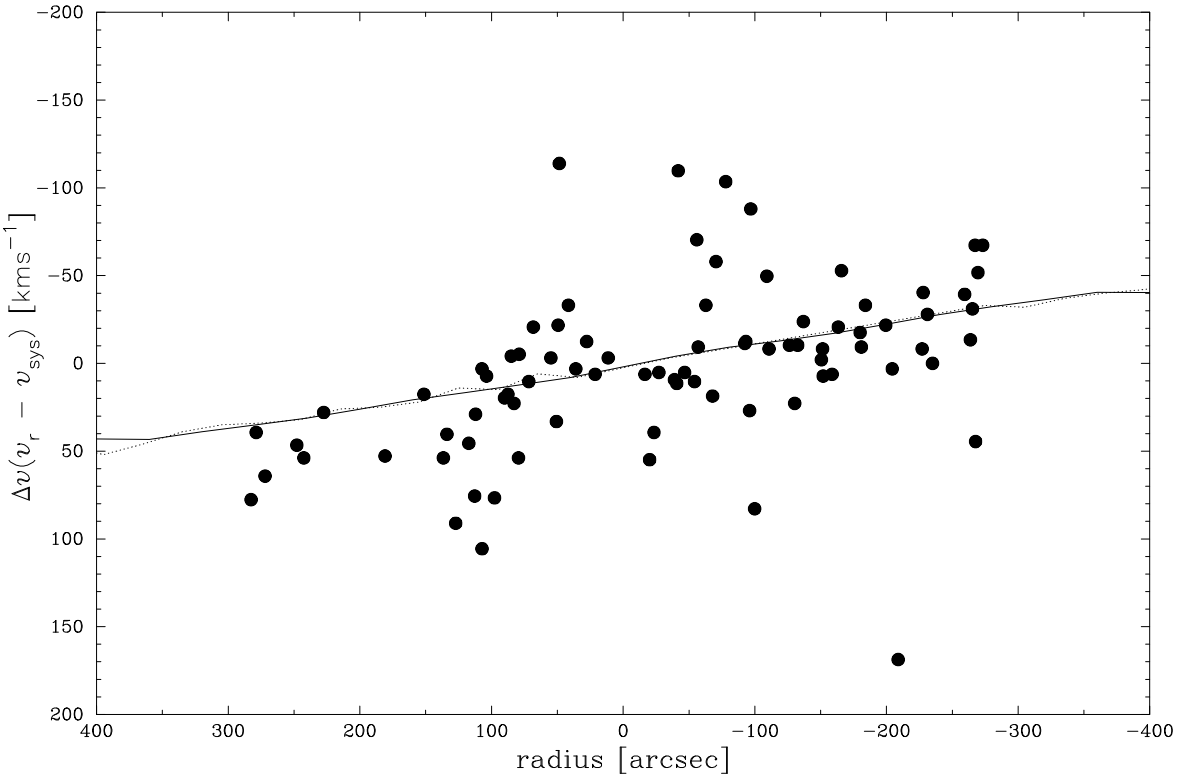

Fig. 15.— Stellar radial velocities, as a function of radius along the major axis of NGC 3109, corrected to the systemic velocity a 402 kms^{-1}. The median 1-σ (internal) uncertainty is 19 kms^{-1}. Also shown are rotation curves from H I (Jobin & Carignan 1990,solid line) and Hα (Blais-Ouellette et al. 2001,dotted line).

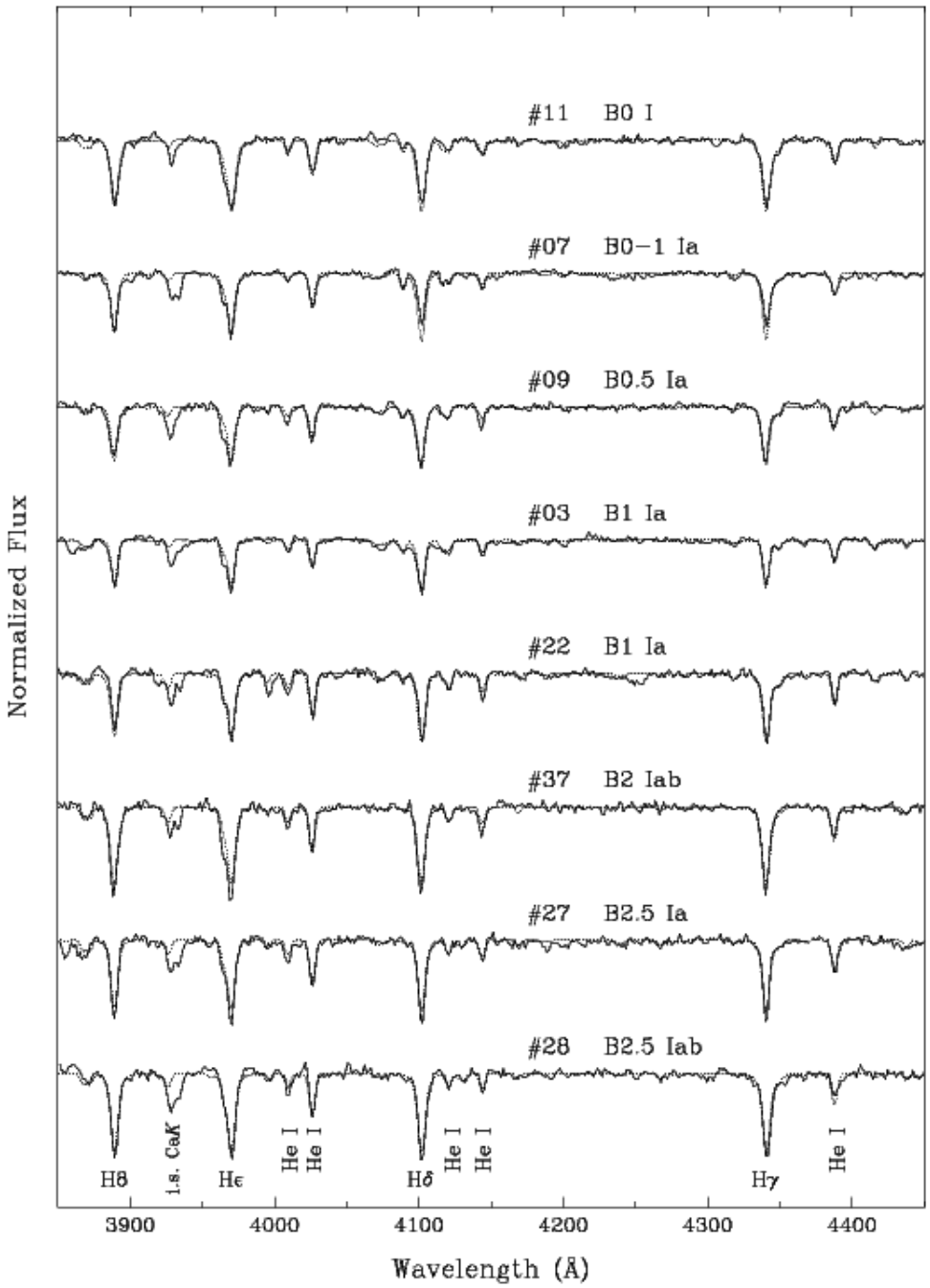

Fig. 16.— FORS spectra ($\lambda\lambda$3850-4450 Å) of B-type supergiants in NGC 3109 (solid lines) compared with the adopted FASTWIND models (dotted lines). In addition to the Balmer lines, the He I $\lambda\lambda$4009, 4026, 4121, 4143, 4388 lines are marked. Most of the absorption $\sim\lambda$3933 Å arises from the interstellar Ca K line.

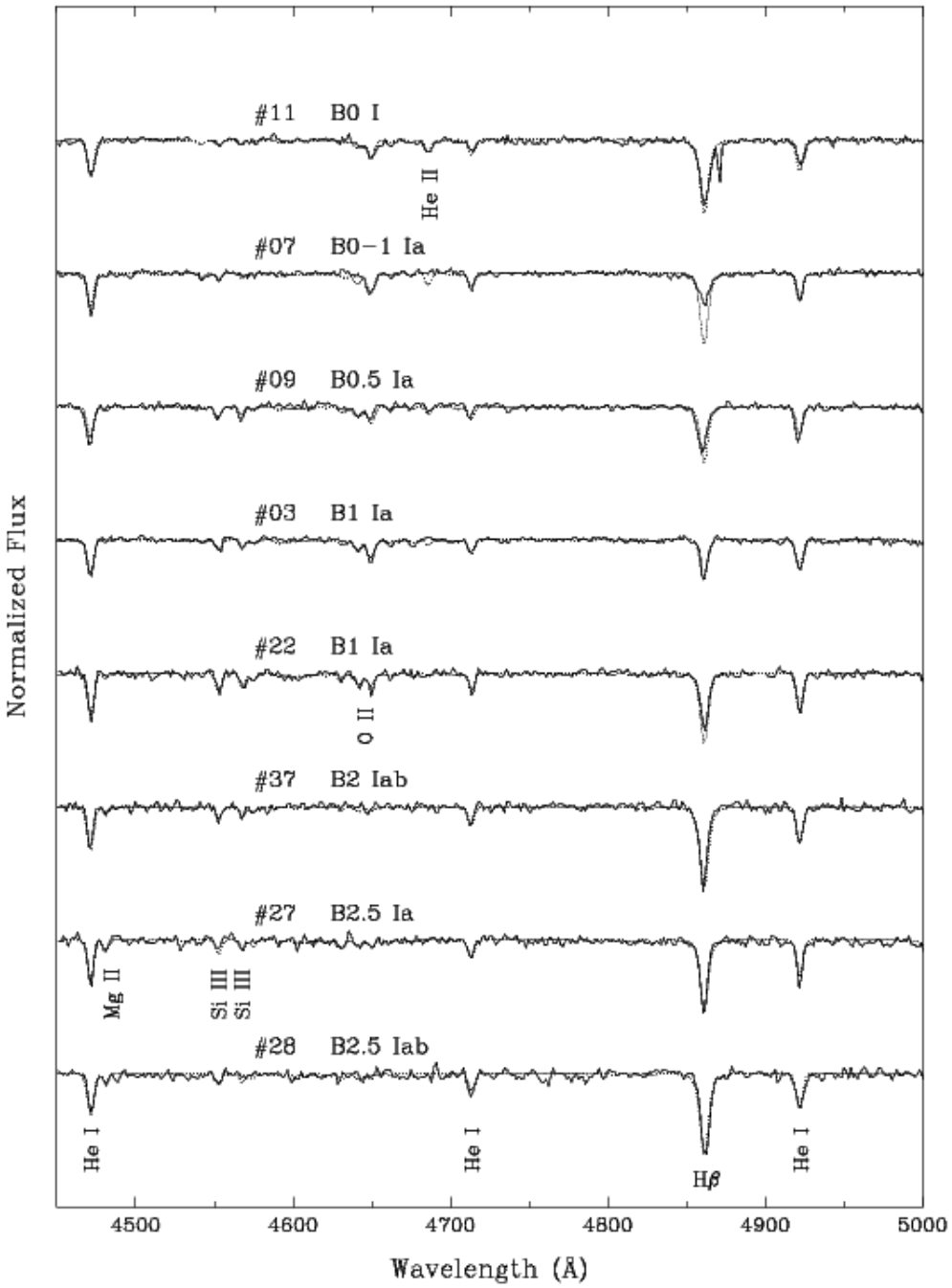

Fig. 17.— FORS spectra ($\lambda\lambda$4450-5050 Å) of B-type supergiants in NGC 3109 (solid lines) compared with the adopted FASTWIND models (dotted lines). The identified absorption lines in the spectrum of star #28 are He I $\lambda\lambda$4471, 4713, 4922, and Hβ; star #27: Mg II λ4481, Si III $\lambda\lambda$4553-4567; star #22: O II $\lambda\lambda$4640-4650; star #11: He II λ4686.

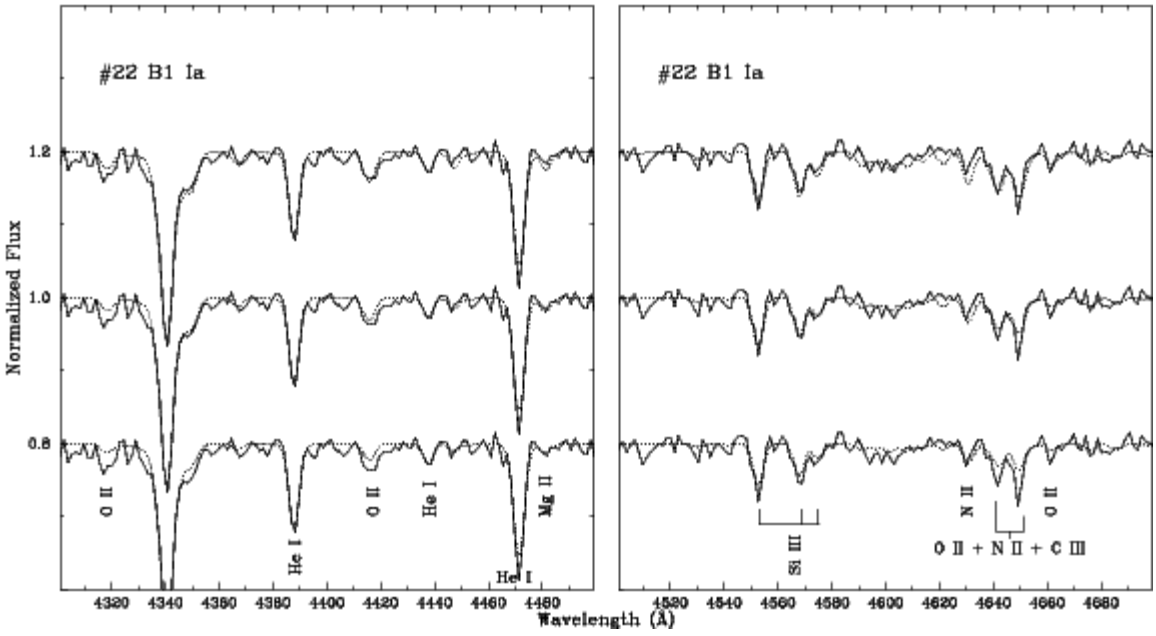

Fig. 18.— Comparison of FORS spectrum of star #22 (solid lines) with FASTWIND models in which the metallic abundances are ±0.2 dex compared to the adopted values (upper and lower spectra respectively). The identified lines are O II $\lambda\lambda$4317-19, 4415-17, 4661; He I $\lambda\lambda$4388, 4438, 4471; Mg II λ4481; Si $\lambda\lambda$4552-68-75; N II λ4631; and the O II +N II +C III blend at λ4650.

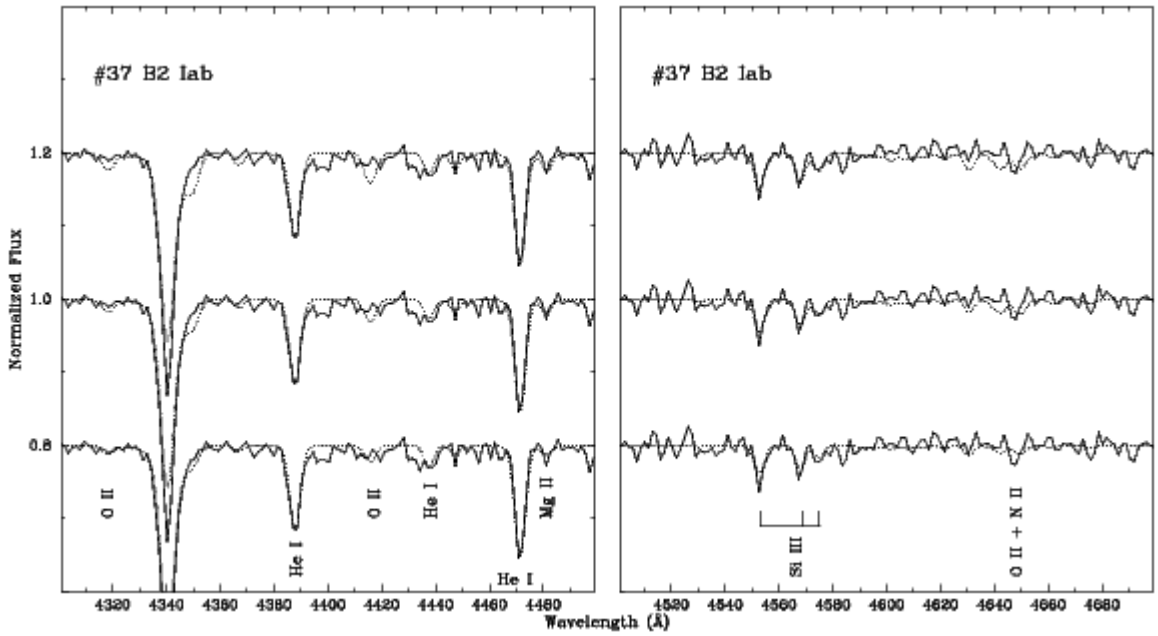

Fig. 19.— Comparison of FORS spectrum of star #37 (solid lines) with FASTWIND models in which the metallic abundances are ±0.2 dex compared to the adopted values (upper and lower spectra respectively).

This figure "f2.jpg" is available in "jpg" format from:

http://arXiv.org/ps/astro-ph/0612114

This figure "f3.jpg" is available in "jpg" format from:

http://arXiv.org/ps/astro-ph/0612114

This figure "f4.jpg" is available in "jpg" format from:

http://arXiv.org/ps/astro-ph/0612114